Journal of Materials Chemistry A

ROYAL SOCIETY OF CHEMISTRY

PAPER

View Article Online
View Journal | View Issue

Cite this: J. Mater. Chem. A, 2025, 13, 40337

Ruddlesden–Popper $Y_2Ti_2O_5S_2$/SWCNT composite anode: durable cycling and ultrafast lithium-ion storage for hybrid supercapacitors

Etsuro Iwama, *[abc] Shintaro Aoyagi,[a] Tatsuro Aoyama,[a] Ami Kudo,[a] Keita Okazaki,[a] Daichi Akiyama,[a] Keisuke Matsumura,[ab] Naohisa Okita,[ab] Kazuaki Kisu,[a] Wako Naoi,[d] Patrick Rozier,[bef] Patrice Simon[bef] and Katsuhiko Naoi *[abcd]

$Y_2Ti_2O_5S_2$ (YTOS) is a unique cation-deficient Ruddlesden–Popper structured material composed of alternating perovskite-like slabs (TiO_5S octahedra) and rock-salt $[Y_2S_2]^{2+}$ layers. Despite its potential for lithium-ion storage, research on YTOS as an energy storage material remains limited, underscoring its novelty and unexplored capabilities. The addition of 1 wt% single-walled carbon nanotubes (SWCNTs) significantly improved the electrochemical performance of YTOS, resulting in enhanced capacity, superior output characteristics, and improved cycle stability compared to the pristine material. The resulting composite demonstrates superior rate capability (up to 230C) and outstanding cycleability, retaining 95% of its capacity even after 1000 cycles. *Operando* XRD and Ti K-edge XAFS analyses reveal fully reversible orthorhombic-tetragonal phase transitions and stable Ti^{3+}/Ti^{4+} redox activity during 500 cycles, while unchanged Y K-edge spectra confirm the structural stability conferred by the yttrium sublattice. Hybrid supercapacitor full cell assemblies with activated carbon (YTOS||AC) display minimal polarization and remarkable durability over 10 000 cycles at 10C, highlighting the material's suitability for high-power capability. This work presents a promising approach for developing high-performance energy storage materials, as the YTOS anode offers both high energy density and excellent cycle life, making it an excellent candidate for advanced lithium-ion batteries and hybrid supercapacitors.

Received 3rd July 2025
Accepted 2nd October 2025

DOI: 10.1039/d5ta05379j

rsc.li/materials-a

Introduction

$Y_2Ti_2O_5S_2$ (YTOS) is an $n = 2$ Ruddlesden–Popper (RP)-type layered oxysulfide, commonly acknowledged as a cation-deficient or empty perovskite material.[1–3] The crystal structure of RP is composed of alternating AB-stacking layers: perovskite-like slabs formed by corner-sharing TiO_5S octahedra (A) and rock-salt-type $[Y_2S_2]^{2+}$ layers (B)[4,5] (Fig. S1). This layered architecture forms a highly ordered two-dimensional framework for lithium ion (Li^+) conduction. The central $[TiO_5S]$ octahedral layer creates interconnected diffusion channels for Li^+ transport as well as electronic conduction, while yttrium atoms are 9-fold coordinated with four oxygen and five sulfur atoms, contributing to structural robustness.[3,5–8] Unlike traditional perovskite oxides, the cation-deficient layered nature of YTOS facilitates ionic diffusion.[8] Additionally, the presence of sulfur in the structure modifies the electronic environment, potentially improving its in-plane electrical conductivity.[7,8] These features suggest that YTOS could be a promising candidate for energy storage, especially as an anode material for lithium-ion batteries and hybrid supercapacitors.

Early topochemical studies led by Simon J. Clarke established chemistry-dependent alkali-ion insertion in YTOS; first Na^+,[1,9] later Na^+/K^+,[10] and subsequently Li^+.[4] Hyett *et al.* chemically introduced Li^+ into the YTOS lattice and, using neutron diffraction, demonstrated that Li^+ occupies square-planar, 4-coordinated oxygen sites (LiO_4) rather than the sterically unfavorable 12-coordinate sites (LiO_8S_4) associated with the cation-deficient framework.[4] In comparison, Na chemically inserts either into the YO_5S slabs (α-phase, at 600 °C *via* Na vapor) or the Y_2S_2 rock-salt layers (β-phase, at <50 °C *via* Na naphthalide in THF), while K inserts exclusively into the rock-salt layers over a broad temperature range (−78 °C to 400 °C). Unlike Na^+ and K^+, Li^+ intercalates reversibly into the YO_5S perovskite slabs owing to its smaller ionic size. Electrochemical study reported by Oki *et al.*[11] in 2015 further demonstrated the

[a]Department of Applied Chemistry, Tokyo University of Agriculture and Technology, 2-24-16 Naka-cho, Koganei, Tokyo 184-8588, Japan. E-mail: iwama@cc.tuat.ac.jp; k-naoi@cc.tuat.ac.jp
[b]Institute of Global Innovation Research, Tokyo University of Agriculture and Technology, 2-24-16 Naka-cho, Koganei, Tokyo 184-8588, Japan
[c]Advanced Capacitor Research Center, Tokyo University of Agriculture and Technology, 2-24-16 Naka-cho, Koganei, Tokyo 184-8588, Japan
[d]Division of Art and Innovative Technologies, K & W Inc., 1-3-16-901 Higashi, Kunitachi, Tokyo 186-0002, Japan
[e]CIRIMAT, Université de Toulouse, CNRS, 118 Route de Narbonne, Toulouse Cedex 9 31062, France
[f]Réseau sur le Stockage Électrochimique de l'Energie, RS2E FR CNRS 3459, 33 Rue Saint Leu, Amiens Cedex 80039, France

reversible, stepwise Li^+ intercalation, manifested as multiple potential plateaus between 1.5 and 0.1 V *vs.* Li/Li^+. These plateaus arise from sequential Ti^{3+}/Ti^{4+} redox steps, yielding an average operating potential of *ca.* 0.8 V *vs.* Li/Li^+ and a theoretical capacity of 128 mA h g^{-1}. In 2021, McColl *et al.*[2] substantiated the previous findings through DFT and *ab initio* molecular dynamics, revealing that Li^+ is thermodynamically stabilized at the square-planar LiO_4 sites, while migration proceeds through transient occupation of the 12-coordinated LiO_8S_4 sites. This pathway yields low migration barriers (20–64 meV), markedly smaller than those of typical Ti-based intercalation materials such as $Li_4Ti_5O_{12}$ (LTO, 200–600 meV),[12,13] thereby enabling rapid two-dimensional transport within the TiO_5S slabs, even in micron-scaled particles. It was also exemplified that increasing Li^+ content ($x > 1$ in $Li_xY_2Ti_2O_5S_2$) significantly enhances the electrical conductivity: from *ca.* 5 mS cm^{-1} at $x = 0.2$ to 50 mS cm^{-1} at $x = 2.0$.[11] This increase in conductivity is accompanied by a transition of metallic behavior, evidenced by Pauli paramagnetism observed between 5 and 300 K,[2] as supported by DFT calculations.[2,4] Moreover, recent *ex situ*/*in situ* X-ray diffraction has uncovered a reversible two-phase reaction between the tetragonal (*I*4/*mmm*) and orthorhombic (*Immm*) phases at the 0.30–0.35 V plateau, with <5% unit-cell volume change.[14]

Despite its promising characteristics—particularly high ionic and electronic conductivity—research on the high-rate electrochemical performance of YTOS remains limited. This gap in the literature highlights both the novelty of YTOS and its significant untapped potential for use in advanced energy storage systems. The unique crystal structure and mixed conduction pathways of YTOS make it a strong candidate for high-power applications, but fundamental challenges in realizing its full potential remain. These include issues related to long-term cycling stability and the lack of well-optimized electrode fabrication methods that can preserve its intrinsic properties.

In this study, we address these critical challenges through a comprehensive investigation of the electrochemical behavior of bulk YTOS, with particular focus on engineering strategies that avoid nanosizing. To probe the intrinsic ionic transport characteristics, we employ cavity microelectrode analysis, which allows for localized electrochemical measurements within a well-defined microstructure. This technique provides valuable insight into ion mobility and reaction kinetics, enabling us to assess YTOS performance independent of extrinsic factors such as particle size and surface area modifications. Rather than relying on nanoscale engineering to enhance performance, our approach emphasizes the optimization of electrode design. Single-walled carbon nanotubes (SWCNTs) are introduced as high-efficiency conductive additives to facilitate electronic percolation throughout the electrode matrix. Furthermore, a customized binder system based on a carboxymethyl cellulose–styrene butadiene rubber (CMC-SBR) formulation is employed to ensure mechanical integrity and uniform dispersion of active materials during cycling. This integrated strategy enables a clearer understanding of the intrinsic limitations and potential of YTOS as an energy storage material without extensive nano-structuring.

Experimental

$Y_2Ti_2O_5S_2$ was synthesized by a solid-state reaction (Fig. 1 [Left]). Titanium metal, sulfur, rutile-type titanium dioxide (TiO_2), and yttrium oxide (Y_2O_3), all obtained from Kojundo Chemical (99.9%), were used as precursor materials. To prevent contamination and oxidation, all handling of precursor materials, including weighing, mixing, and pelletizing, was performed within a glove box under an inert gas atmosphere. TiS_2 was first synthesized by heat-treating a mixture of Ti and S *in vacuo* at 600 °C for 96 h. Subsequently, all raw materials for YTOS were mixed in a molar ratio of $Y_2O_3 : TiO_2 : TiS_2 = 1.000 : 0.975 : 1.025$ to compensate for sulfur loss during the high-temperature synthesis. Before pelletization, the commercial TiO_2 and Y_2O_3 powders were pre-dried *in vacuo* at 120 °C for 24 h in the glove box to remove residual moisture that could otherwise interfere with the reaction and lead to phase impurities. The homogenized powder mixture was then pressed into pellets to ensure uniform reaction during the subsequent sintering process. The pellets were then placed into an acid-proof digestion vessel and vacuum-sealed at approximately 30 Pa to minimize sulfur loss and ensure a controlled reaction environment. The reaction proceeded in an electric furnace with a controlled heating program. The temperature was initially increased at a rate of 12 °C h^{-1} to allow slow diffusion of reactants, preventing the formation of undesirable intermediate phases. At a later stage, the ramping rate was increased to 100 °C h^{-1} to promote efficient phase transformation. After reaching the target temperature, the sample was held at high temperature (1100 °C) for a sufficient duration (96 h) to ensure complete reaction to promote S/O exchange and long-range ordering of the RP framework. The sintering process to obtain YTOS gave 97.1% yield, while TiS_2 synthesis gave 95.2% yield, calculated as isolated product mass over theoretical stoichiometric mass.

The synthesized material and electrodes were characterized using several techniques. X-ray diffraction (XRD) measurements were performed using a Rigaku Smart Lab system to analyze the crystallographic structure. X-ray photoelectron spectroscopy (XPS) was conducted using a JEOL JPS-9020 to study surface composition and chemical states. Transmission electron microscopy (TEM) was carried out using a Hitachi H-9500 to observe the microstructure at high resolution. The surface morphology and elemental distribution were examined using a Hitachi S-5500 scanning electron microscope (SEM) and a Hitachi HD-2700 scanning transmission electron microscope (STEM). Thermogravimetric-differential thermal analysis (TG-DTA) was performed with an EXTRA TG/DTA6000 (SII Nano-Technology) to investigate thermal stability and phase transitions. The electrochemical performance of the synthesized material was evaluated using a charge/discharge system (Hokuto Denko SD8) for constant current charge/discharge modes and an ALS660A electrochemical analyzer (BAS) and VSP-300 Potentiostat (Biologic) for cyclic voltammetry.

For electrode fabrication, poly(vinylidene difluoride) (PVdF 9305, Kureha Corp.), carboxymethyl cellulose (CMC Celogen WS-C, DKS Corp.), and styrene–butadiene rubber (SBR TRD-

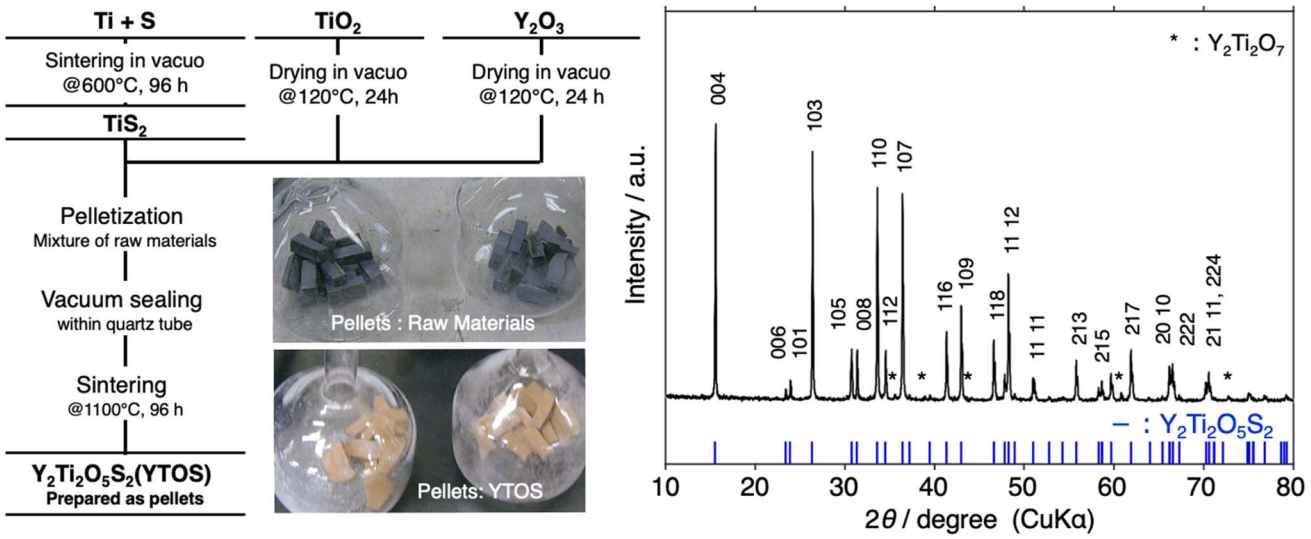

Fig. 1 [Left] Synthesis scheme of $Y_2Ti_2O_5S_2$ (YTOS). The synthesis begins with a carefully prepared precursor mixture of TiO_2, TiS_2, and Y_2O_3, which is thoroughly ground to ensure homogeneity before being pelletized under high pressure. The resulting pellets are then vacuum sealed in a quartz tube to maintain a controlled atmosphere and prevent contamination. The sealed tube is subsequently sintered at 1100 °C for 96 h, allowing the solid-state reaction to proceed and yielding yellow-colored YTOS pellets with a well-ctstallized structure. [Right] XRD patterns of the synthesized YTOS, confirming its phase purity and crystallographic structure. The major diffraction peaks correspond to the reference pattern for YTOS (*I*4/*mmm*), verifying a tetragonal lattice with refined lattice constants of $a = 3.777$ Å and $c = 22.78$ Å. A minor impurity phase, $Y_2Ti_2O_7$, is also detected (denoted by asterisks), suggesting a slight loss of sulfur (S) atoms from the YTOS crystal structure. This minor deviation may result from sulfur volatility or slight variations in synthesis conditions. Despite this, the predominant presence of the YTOS phase indicates the successful formation of the target material, highlighting its structural integrity and potential for further investigation.

2001, JSR Corp.) were used as binders. The YTOS was mixed with these binders of CMC (2.5 wt%)–SBR (2.5 wt%), 20 wt% of conductive additives (acetylene black: AB) with or without 1 wt% of SWCNTs (TUBALL, Kusumoto Chemicals) to form a uniform slurry, which was coated onto carbon-coated copper foil (8 μm), supplied by Nippon Graphite. The coated electrodes were then vacuum dried and processed for electrochemical testing. The loading mass of electrodes were controlled to be 1.5–2.0 mg cm^{-2}. The coated YTOS electrodes were assembled with Li metal in CR2032-type coin cells. The electrolyte was 1 M lithium tetrafluoroborate ($LiBF_4$) in a mixture of ethylene carbonate and dimethyl carbonate (EC : DMC = 1 : 1 in vol%), battery grade (Kishida Chemical), a commonly used system noted for its high moisture stability. This choice is especially relevant for hybrid capacitor cells employing activated carbon (AC) positive electrodes in hybrid capacitor configurations, which typically retain trace adsorbed water (~50 ppm)[15] that can otherwise trigger the electrolyte degradation. Cycling tests were performed within a potential window of 0.1–2.0 V *vs.* Li/Li^+. For laminate-type hybrid supercapacitors, the YTOS negative electrode was paired with an AC (YP-50, Kuraray) positive electrodes (AC : AB : PVdF = 7.5 : 1.5 : 1) coated on carbon-coated aluminum foil (20 μm, Nippon Graphite). A negative-to-positive (N/P) electrode mass ratio of 2 : 1 was applied to optimize the balance.

Results and discussion

The crystal structure of the synthesized YTOS material was first evaluated by XRD patterns as shown in Fig. 1 [Right]. The major diffraction peaks observed in the XRD patterns were successfully indexed to the simulated XRD patterns of YTOS (*I*4/*mmm*), as previously reported by Hyett *et al.*,[4] with refined cell parameters $a = 3.777$ Å and $c = 22.78$ Å consistent with reported ones ($a = 3.763$–3.780 Å, $c = 22.73$–22.82 Å).[2,11] In addition to the primary peaks corresponding to the YTOS phase, minor peaks are also detected in the XRD patterns. These minor peaks correspond to trace amounts of the impurity phase $Y_2Ti_2O_7$ formed during the synthesis process. Nonetheless, the overall purity of the synthesized YTOS material is still considered high, and the presence of this minor impurity may not significantly detract from the material's performance. The thermogravimetric (TG) curve of YTOS under N_2 (Fig. S2) demonstrates excellent thermal stability up to 700 °C, with the weight remaining essentially constant in the 200–700 °C range. This stable plateau confirms the robustness of the layered RP framework and the absence of volatile species or structural decomposition under these conditions. Above 700 °C, a gradual mass loss is observed, suggesting the onset of sulfur volatilization and partial destabilization of the sulfide-oxide lattice. Beyond 1000 °C, the TG profile shows an abrupt weight drop, which we attribute to extensive sulfur vaporization and the subsequent collapse of the layered sulfide structure into the oxide phase $Y_2Ti_2O_7$ (see inset in Fig. S2). These results clarify the intrinsic thermal stability limits of synthesized YTOS near 700 °C: the structure remained essentially intact below this temperature, while sulfur volatilization and subsequent phase transformation emerged at higher temperature.

The morphology and size distribution of the synthesized YTOS particles were investigated using scanning electron microscopy (SEM) and dynamic light scattering (DLS) analysis.

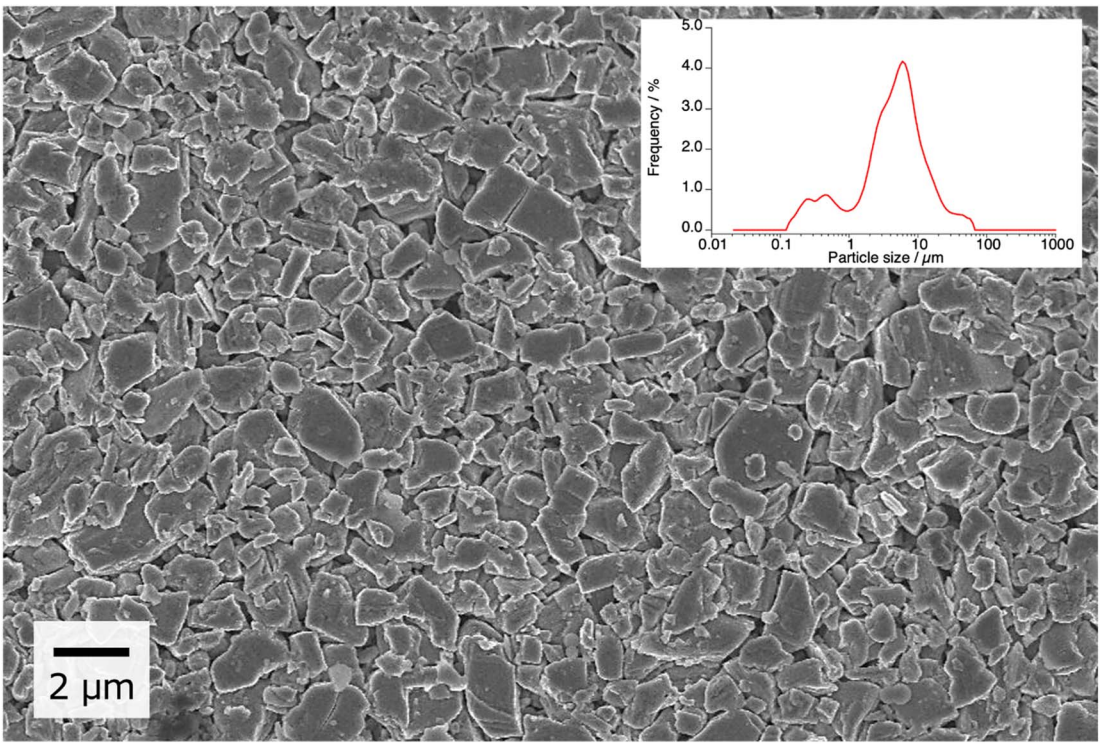

Fig. 2 Scanning electron microscopy (SEM) images of the synthesized $Y_2Ti_2O_5S_2$ (YTOS) particles, showing their characteristic plate-like morphology. The observed particle sizes range from approximately 0.5 to 3 μm, with relatively uniform distribution. The individual particles appear well-defined, with minimal agglomeration, suggesting that the synthesis process successfully yielded distinct YTOS crystallites. The plate-like structure may be indicative of anisotropic growth tendencies, potentially influenced by the layered nature of the material or the conditions employed during synthesis. [Inset] Particle size distribution analysis of YTOS dispersed in distilled water, indicating that, in the absence of ultrasonication, some particle clusters exceed 30 μm in size, likely due to mild aggregation effects. However, after subjecting the dispersion to ultrasonication, the overall particle size distribution shifts toward smaller values, aligning well with the size range observed in the SEM images. This reduction in larger particle sizes suggests that the weakly aggregated YTOS particles readily separate under ultrasonic treatment, further confirming the relatively loose interparticle interactions.

SEM imaging, as shown in Fig. 2, reveals that the YTOS particles exhibit a characteristic plate-like morphology, indicative of a layered structure, with particle sizes ranging from approximately 0.3 to 3 μm. DLS analysis of the aqueous YTOS dispersion (Fig. 2 inset) shows a slightly broader size distribution (0.3–10 μm) compared to that observed in the SEM image, reflecting moderate agglomeration of 3–4 primary particles in the dispersed state. Despite the aggregation observed in dispersion, both techniques consistently confirm that the primary YTOS particles are in the micrometer range. The anisotropic plate-like shape observed by SEM likely originates from the intrinsic layered structure of YTOS. Notably, the obtained *c*-axis lattice parameter of the synthesized YTOS (c = 22.78 Å) is much smaller compared to the simulated (c = 28.20 Å)[2] and experimentally reported values for YTOS samples synthesized below 800 °C (c = 29.18–29.62 Å).[16] This pronounced structural anisotropy arises from the intrinsic layered nature of YTOS, which crystallizes in the tetragonal *I*4/*mmm* space group. The crystal architecture features alternating $[Y_2S_2]^{2+}$ rock-salt-type layers and $[TiO_5S]$ perovskite-like slabs stacked along the *c*-axis. Such an interlayered framework can hinder ion mobility along the *c*-axis under synthetic conditions, thereby imposing structural constraints on crystal growth in that direction. In contrast, the continuous network of corner-sharing TiO_6 octahedra within the (*a*–*b*) plane facilitates lateral expansion. Consequently, crystal growth predominantly proceeds within the (*a*–*b*) plane, yielding well-defined plate-like or rectangular prismatic morphologies characterized by a compressed *c*-axis compared to the theoretical value. The markedly shortened *c*-axis parameter observed in the present sample synthesized at 1100 °C is therefore consistent with this two-dimensional growth tendency governed by the layered YTOS framework.

The schematic crystal structure of YTOS, depicted in Fig. 3, elucidates its unique atomic layering, comprising alternately stacked perovskite-like slabs and rock-salt-type layers, each contributing distinctively to the material's transport properties. The perovskite-like slabs serve as primary pathways for ionic conduction, facilitating the migration of charge carriers such as lithium ions. Within these layers, Ti ions are coordinated in distorted TiO_5S octahedra. The Ti–S bond, with a length of approximately 2.89 Å, is significantly longer than the Ti–O bonds (~1.81 Å), reflecting reduced orbital overlap between Ti d- and S p-orbitals. This weakened out-of-plane interaction likely hinders electron transport along the *c*-axis, resulting in pronounced electronic anisotropy.[3,7,17] Conversely, although the Ti–O bond is formally more ionic than the Ti–S bond due to the

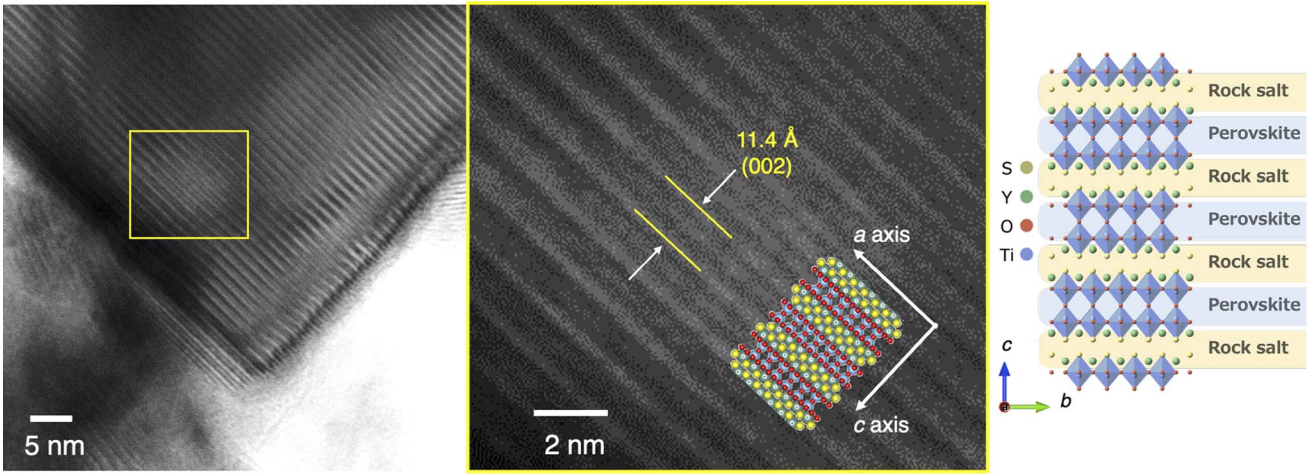

Fig. 3 [Left] High-resolution transmission electron microscopy (HRTEM) images of YTOS crystals, showcasing well-defined lattice fringes corresponding to the (002) plane. [Right] A magnified view of the selected area (highlighted by the yellow square), where the clear visibility of these fringes confirms the high crystallinity of the synthesized YTOS and provides insight into its atomic-scale structural arrangement. [Inset] A schematic representation of the YTOS crystal structure, depicting alternately stacked perovskite-like slabs and rock-salt layers. The perovskite phase, which contains the ion-conducting layers, is interspersed with rock-salt layers that primarily facilitate electronic conduction.

larger electronegativity difference between Ti and O, the Ti–O network within the *a*–*b* plane exhibits stronger orbital overlap and shorter bond distances. These features promote more effective electron delocalization in-plane. Electronic localization function analyses,[16] support a delocalized, gas-like electron distribution confined within the [TiO_5S] perovskite-like slabs, indicative of a structure that favors lateral charge transport. The synergistic contribution of these structural elements imparts YTOS with both high ionic conductivity and directionally enhanced electronic conductivity—key features for dual-function electrode materials.

To further validate the structural composition and elemental distribution of YTOS, scanning transmission electron microscopy (STEM) coupled with elemental mapping (Fig. S3) was employed. The elemental maps confirm the successful incorporation of oxygen (O), sulfur (S), titanium (Ti), and yttrium (Y) within the crystal lattice. The corresponding elemental maps exhibit a homogeneous spatial distribution of these constituent elements, supporting the presence of an ordered, alternating arrangement of rock-salt layers and perovskite-like slabs.

Electrochemical performance

To evaluate the electrochemical performance of YTOS, galvanostatic charge–discharge cycling tests were conducted. A comparative analysis was carried out between two electrode configurations: one containing SWCNTs as a conductive additive and one without. Two XPS spectra for YTOS with (blue) and without SWCNT (red) shown in Fig. S4 exhibit an almost complete overlap, indicating that the overall surface chemical environments are essentially identical. The only differences are the additional peaks that can be attributed to the binders employed: CMC-SBR in combination with SWCNTs in one case, and PVdF without SWCNTs in the other. These binder-related features account for the minor deviations observed, while the active material itself remains chemically indistinguishable between the two electrodes. The impact of SWCNTs in mitigating resistive losses and enhancing isotropic electron transport was assessed by monitoring changes in specific capacity, rate performance, and cycle stability. The incorporation of SWCNTs was anticipated to improve electronic conductivity by promoting more efficient electron percolation and uniform charge distribution within the electrode matrix. As shown in the inset of Fig. 4 [Left], at a current density of 0.1 A g^{-1}, the YTOS electrode containing 1 wt% SWCNT delivered a specific capacity of 112 mA h g^{-1} per electrode. This corresponds to the 121 mA h g^{-1} per YTOS after subtracting the capacity contribution from conductive agents (AB and SWCNT), which is approximately 95% of the theoretical capacity (128 mA h g^{-1}) and consistent with reported values (126–128 mA h g^{-1}) in prior studies.[11,14] This high utilization indicates that the presence of minute impurity ($Yi_2Ti_2O_7$) detected in XRD patterns (Fig. 1 [Right]) has a negligible effect on the electrochemical performance of the YTOS anode.

To assess the rate capability of YTOS, the cells were subjected to galvanostatic cycling at various current densities ranging from 0.1 to 30 A g^{-1}, corresponding to C-rates from approximately 0.8C to over 200C as shown in Fig. 4 [Left]. Analysis of the specific capacity retention at increasing delithiation rates provided insights into the kinetic limitations of lithium transport. Remarkably, even without SWCNTs, the YTOS/AB electrode (80 : 20 wt%) retained over 80% of its initial capacity at 20 A g^{-1} (~150C) compared to 0.1 A g^{-1}. Upon incorporation of 1 wt% SWCNTs, the C-rate capability was further enhanced, achieving ~90% capacity retention at 30 A g^{-1} (~230C). This exceptional high-rate performance underscores the rapid lithium-ion diffusion and low charge-transfer resistance within the YTOS structure.

Long-term galvanostatic cycling tests were carried out to assess the durability of the YTOS anode under extended charge–

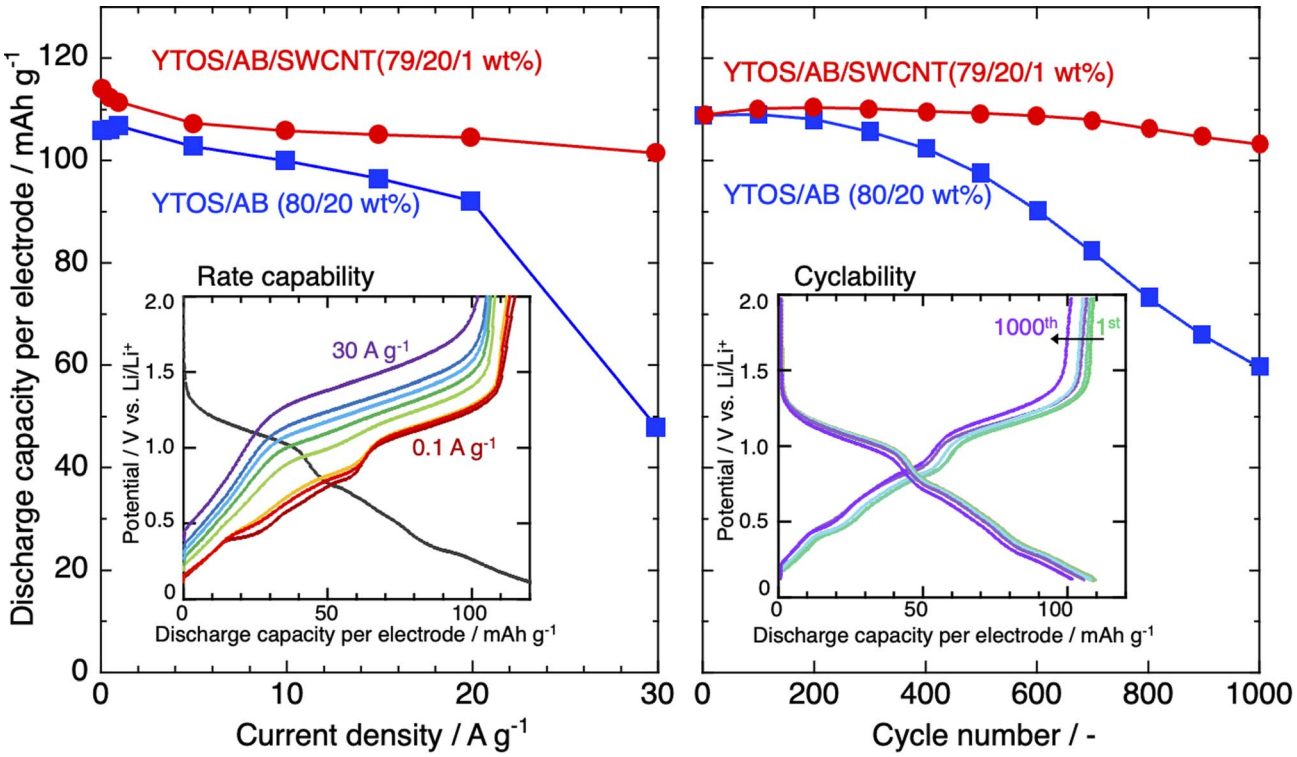

Fig. 4 [Left] Discharge rate capability and [Right] cycling performance of the YTOS electrode with or without 1 wt% SWCNT. The electrochemical performance was evaluated using 2032-coin cells in a Li/YTOS half-cell configuration, employing 1 M $LiBF_4$ in ethylene carbonate (EC) and dimethyl carbonate (DMC) (50 : 50 in vol%) as the electrolyte. Discharge capacity is presented per unit electrode weight. To assess the rate capability, the cells were subjected to a range of discharge rates, with current densities varying from 0.1 to 30 A g^{-1}. [Left inset] Discharge curves for YTOS/AB/SWCNT (79/20/1 in wt%) electrode with current densities varying from 0.1 to 30 A g^{-1}. The cycling performance (3.2C/3.2C, *i.e.* 0.4/0.4 A g^{-1}) was examined up to 1000 cycles to investigate long-term stability, capacity retention, and the overall electrochemical durability of the YTOS electrode. Throughout the experiments, the voltage range was maintained between 0.1 and 2.0 V to ensure consistent electrochemical evaluation. This window was selected to facilitate lithium insertion/extraction reactions while minimizing side reactions that could negatively impact performance. [Right inset] Representative charge discharge curves for the Li||YTOS/AB/SWCNT (79/20/1 in wt%) cell from 1st to 1000th cycle.

discharge operation (Fig. 4 [Right]). The evolution of capacity with cycle number was monitored to evaluate electrochemical stability and structural resilience. While the RP-type layered framework of YTOS is generally regarded as structurally robust due to its alternating perovskite-like slabs and rock-salt layers, the Ti–S bonds—being longer than the Ti–O bonds—represent a relative point of fragility within the lattice.[16] In the absence of SWCNTs, the electrode exhibited significant capacity fading, retaining only 50% of its initial capacity after 1000 cycles, accompanied by a gradual loss of plateau-like regions in charge discharge curves from the 200th cycle (see also Fig. S5). In contrast, the incorporation of 1 wt% SWCNT dramatically enhanced cycling performance, resulting in 95% capacity retention after 1000 cycles without increase in overvoltage in charge discharge curves (see the inset of Fig. 4 [Right]). This high durability is consistent with the XRD patterns recorded before and after 500 cycles (Fig. S6), which indicate the preserved crystallinity of YTOS. These results underscore the importance of incorporating long-aspect-ratio conductive additives such as SWCNT in mitigating resistive losses and maintaining continuous electron transport—particularly in layered materials like YTOS, where intrinsic anisotropy governs electronic conduction especially in micron-sized particles. To further assess stability under open-circuit conditions, we examined the voltage-relaxation segments in our GITT protocol. After each pulse, the cell rests at open circuit; once the ohmic/concentration drop decays, any residual drift mainly reflects parasitic leakage. As shown in Fig. S7, the voltage stabilizes within a few millivolts (~10 mV) and remains flat during the rest intervals, with nearly identical charge and discharge relaxations. This indicates very low self-discharge and a stable interface, consistent with the high coulombic efficiency and long-term retention described above. A literature comparison of the electrochemical performance of YTOS-based anodes for Li^+ storage is summarized in Table S1. Our YTOS/AB/SWCNT (79/20/1) electrode at decent loading (1.5–2.0 mg cm^{-2}) operates up to 230C (30 A g^{-1}) while retaining ~90% of 0.8C capacity. Cycling stability is also superior: 95% retention after 1000 cycles at 3.2C/3.2C, compared with 71% after 800 cycles at 0.5C/0.5C (Takada *et al.*)[14] and only 30 cycles at 0.02C (Oki *et al.*).[11] Collectively, these results establish ultrahigh-C-rate operation (230C) and long-term durability (1000 cycles) not previously demonstrated for YTOS.

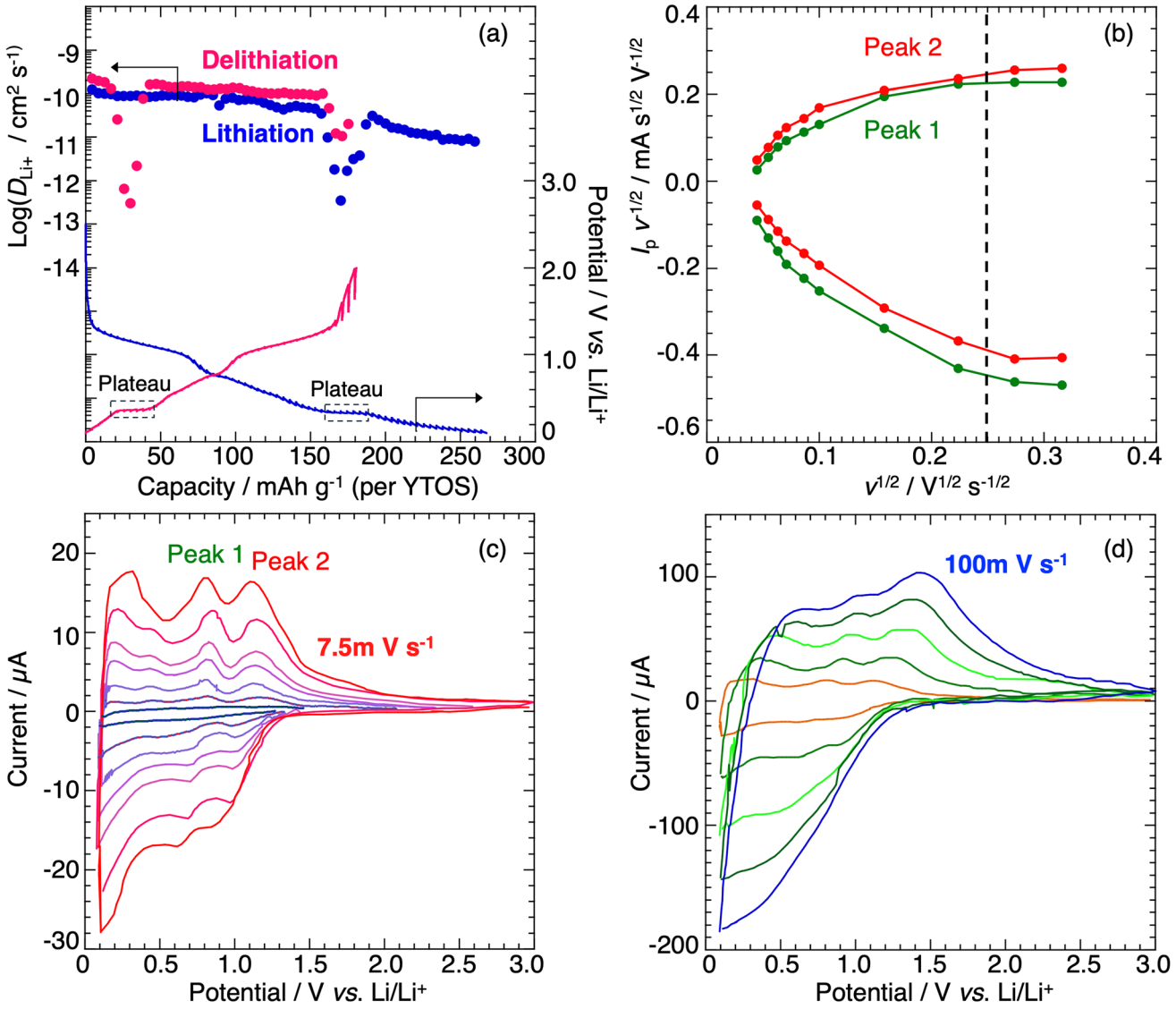

Fig. 5 (a) Diffusion coefficients of Li^+ (D_{Li^+}) with potential curves obtained by GITT measurements using Li/1 $MLiBF_4$/EC + DMC (50 : 50 in vol%)/YTOS 2032-coin half cells. The applied current density was 0.2C, with a loading duration of 10 min followed by a rest period of 2 h at each measurement point. Most of the evaluated values of D_{Li^+} range between 10^{-9} and 10^{-11} cm^2 s^{-1}. The similarity of D_{Li^+} during charge and discharge indicates high reversibility of lithiation/delithiation within YTOS crystal structure. The sudden drops in D_{Li^+} at 20–40 mA h g^{-1} during delithiation (pink) and 160–180 mA h g^{-1} during lithiation (blue) corresponds to the highlighted plateau regions at *ca.* 0.3 V *vs.* Li in charge and discharge curves, indicating the phase transition between orthorhombic and tetragonal structures. (b) Plot of I_p $v^{-1/2}$ *vs.* $v^{1/2}$ from 0.1 mV s^{-1} to 1 V s^{-1} evaluated from the current of peaks 1 and 2 in cyclic voltammograms using cavity microelectrode scanned (c) from 1 to 7.5 mV s^{-1} and (d) from 10 to 100 mV s^{-1}. The dotted line in (b) corresponds to the boundary line of k_1-dominant and k_2-dominant regions. The $v^{1/2}$ value of boundary line, 0.3 $V^{1/2}$ $s^{-1/2}$ is much higher compared to the reported value as a bulk electrode material (0.1 for $LiFePO_4$), showing the ultrafast characteristics of Li^+ accommodation in YTOS.

Charge storage mechanisms and kinetic analysis

The effective transport of Li^+ within YTOS is a key factor in determining its kinetic properties, directly influencing its charge storage efficiency, diffusion dynamics, and overall electrochemical performance. The ability of YTOS to facilitate rapid and reversible Li^+ insertion and extraction is essential for maintaining high-rate capability, minimizing polarization effects, and ensuring long-term structural stability during repeated cycling. Fig. 5(a) presents the diffusion coefficients of Li^+ (D_{Li^+}) as a function of potential, obtained through GITT measurements. The diffusivity results indicate that most of the calculated D_{Li^+} values fall within the range of 10^{-9} to 10^{-11} cm^2 s^{-1}, signifying relatively fast Li^+ transport. Additionally, the diffusion coefficients exhibit nearly identical trends during charge and discharge, suggesting a highly reversible Li^+ insertion and extraction process in YTOS. This reversibility indicates that the crystal structure of YTOS remains stable throughout electrochemical cycling, allowing for efficient Li^+ accommodation with minimal structural distortion. A notable feature observed in the diffusion coefficient profile is the sudden drop in D_{Li^+} at *ca.* 0.3 V

vs. Li/Li^+, coincides with the plateaus both during delithiation and lithiation. This behavior suggests a transformation between tetragonal and orthorhombic phases,[14] which momentarily restricts Li^+ mobility before stabilizing in the new structural configuration. In such plateau regions, Li^+ transport may proceed *via* phase-boundary propagation, and the Weppner–Huggins analysis in GITT[18] can underestimate D_{Li^+} values due to the small change in equilibrium potential on the voltage plateaus after relaxation.[19] Nevertheless, the capacity fraction influenced by this low-D_{Li^+} window is minor (<20 mA h g^{-1}), while most of the operation occurs in single-phase regions where D_{Li^+} remains 10^{-9} to 10^{-11} cm^2 s^{-1} with nearly identical charge/discharge trends. Thus, the observed minima reflect two-phase thermodynamics rather than loss of intrinsic mobility, and they do not limit the demonstrated ultrafast performance. The ability of YTOS to maintain relatively high D_{Li^+} values outside these phase transition regions underscoring its potential as rapid Li^+ diffusion. A cavity microelectrode was used to further explore the Li^+ storage kinetics in YTOS crystal. The total measured current of the obtained cyclic voltammograms (CV) can be deconvoluted into two contributions using the following eqn (1):

$$I_p\ v^{-\frac{1}{2}} = k_1 v^{\frac{1}{2}} + k_2 \quad (1)$$

where I_p, and v stand for the peak intensity in A and the scan rate in V s^{-1}, respectively. The coefficient k_1 corresponds to the non-diffusion-limited surface process, while k_2 reflects the diffusion-limited faradaic reaction.[20,21] Assuming that the obtained current for YTOS is rate-determined by Li^+ diffusion, we plotted the $I_p v^{-1/2}$ using Peak 1 and Peak 2 current against $v^{1/2}$ in Fig. 5(b) from recorded CVs (Fig. 5(c) and (d)).

One of the most significant observations in Fig. 5(b) is the presence of a clear boundary line, represented by the dotted trend, which differentiates the k_1-dominant (surface-controlled) and k_2-dominant (diffusion-limited) regions. The transition occurs at a characteristic $v^{1/2}$ value of approximately 0.25 $V^{1/2}$ $s^{-1/2}$. Compared to conventional materials such as $LiFePO_4$,[20,22] which exhibits a boundary at around 0.1 $V^{1/2}$ $s^{-1/2}$, YTOS demonstrates a much higher threshold, suggesting its ability to accommodate Li^+ at significantly faster rates.

Structural evolution of YTOS during electrochemical cycling

To investigate the structural evolution of YTOS during lithiation and delithiation, *operando* XRD measurements were conducted (see Fig. 6 [Left]). These diffraction patterns reveal phase transitions and lattice modifications that occur as Li^+ ions are inserted into and extracted from the YTOS crystal structure. A more detailed examination of the structural changes is provided in Fig. 6 [Right], which highlights the evolution of the (004) diffraction peak within the narrower 2θ range of 15° to 16.5°. This peak is particularly sensitive to changes in the *c*-axis lattice parameter, making it a useful indicator of volumetric expansion and contraction during Li^+ insertion and extraction. The shifting of the (004) peak position demonstrates a reversible lattice modulation, where a contraction occurs during lithiation, and an expansion is observed during delithiation. This behavior suggests that YTOS accommodates Li^+ in a highly reversible manner, allowing for structural stability throughout the charge–discharge process. The absence of additional diffraction peaks or significant peak broadening further confirms that no major phase decomposition occurs, reinforcing the structural

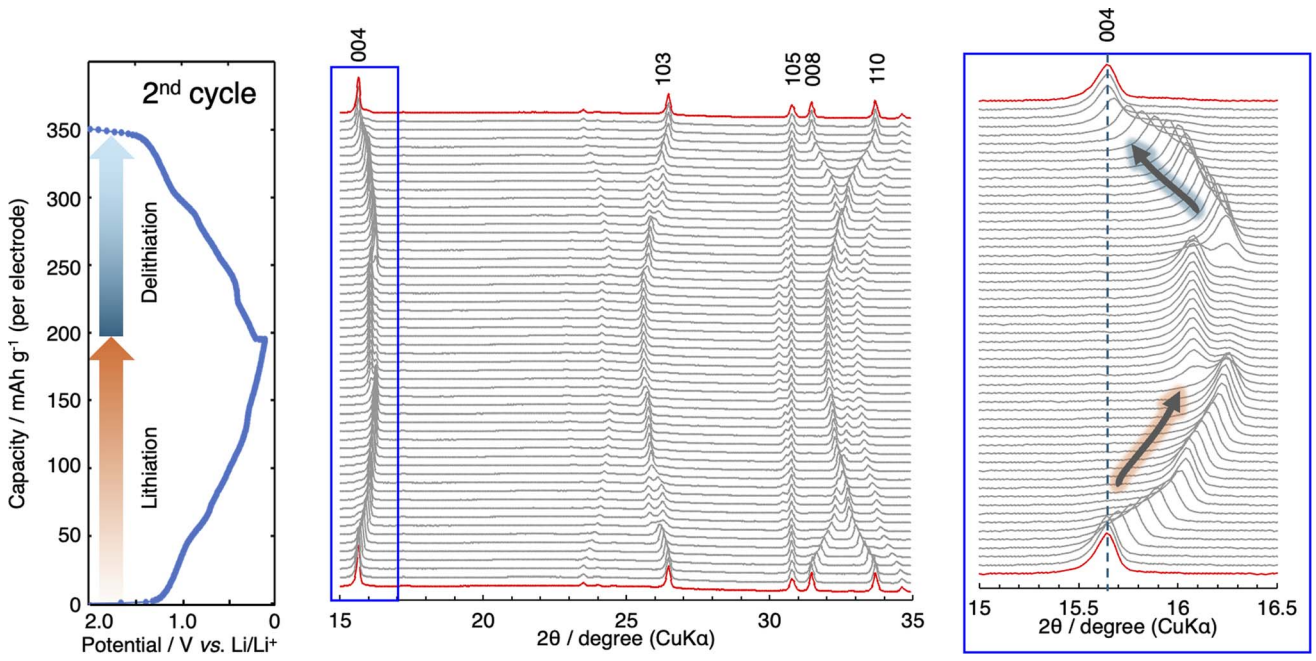

Fig. 6 [Left] *Operando* XRD patterns of YTOS during 2nd cycle recorded between 15° and 35° using X-ray with $\lambda = 1.54$ Å (Cu kα). [Right] Evolution of enlarged XRD patterns between 15° and 16.5°, corresponding to (004) plane, showing reversible crystal change of YTOS during charge and discharge; shrink (Li insertion) and expansion (Li de-insertion) along *c*-axis. Applied current density was 1/10 C-rate.

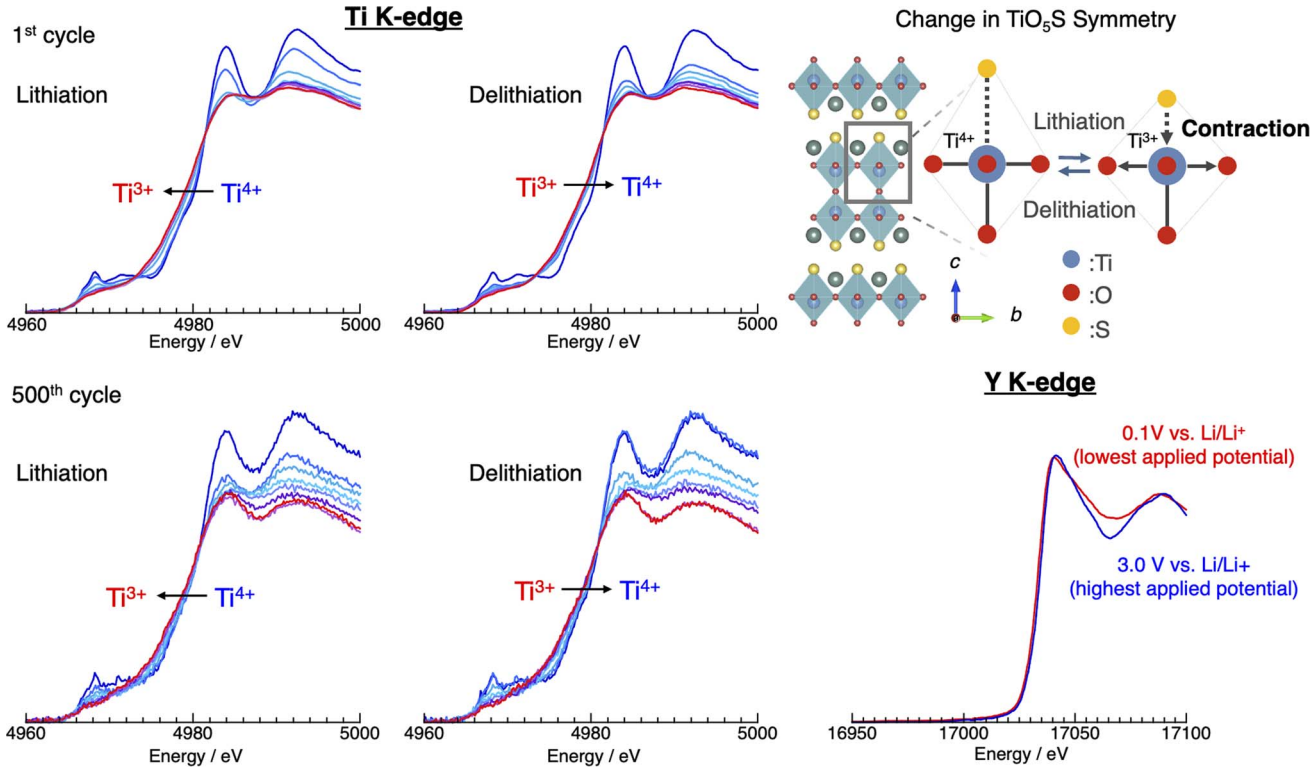

Fig. 7 *Operando* Ti K-edge XAFS spectra of YTOS during the 1st cycle [Top] and 500th cycle [Bottom] along with Y K-edge spectra. During the 1st cycle, Ti K-edge spectra exhibit a reversible energy shift between Ti^{3+} (0.1 V *vs.* Li/Li^+, toward lower energy) and Ti^{4+} (3.0 V *vs.* Li/Li^+, toward higher energy), indicating a reversible Ti^{3+}/Ti^{4+} redox process associated with lithiation and delithiation. The diminished pre-edge peaks around 4968 eV, corresponding to the 1s–3d transition, reflects symmetry around Ti centered in the TiO_5S octahedral coordination [Inset]. This recovery of electronic symmetry aligns well with the *operando* XRD results (Fig. 6), where the vertical TiO_5S octahedron contracts along the *c*-axis (Ti–S bonding), enhancing crystallographic symmetry. Similar spectral shifts are observed in the 500th cycle, indicating the sustained redox reversibility and structural stability (see also Fig. S4), consistent with the long-term cycling performance (Fig. 4 [Right]). In contrast, the Y K-edge spectra, consistent with previously-reported data for yttrium-based compounds ($Y_2Ti_2O_7$ (ref. 37) or Y_2O_3 (ref. 38)), show negligible energy shift between 0.1 V (red) and 3.0 V *vs.* Li/Li^+(blue), confirming that the Ti^{3+}/Ti^{4+} is the predominant redox couple in YTOS upon lithiation/delithiation. Applied current density was 1/10 C-rate, ensuring that the observed spectral features accurately reflect the intrinsic redox behavior of the material.

robustness of YTOS under electrochemical cycling conditions. Interestingly, in contrast to the smooth and continuous peak shifts observed for most reflections, a reversible two-phase peak evolution is evident in the voltage range of 0.3–0.4 V, where sharp features appear in the d*Q*/d*V* plots (Fig. S8). This observation aligns with the sudden drops in the diffusion coefficient (D_{Li^+}) seen in the GITT analysis (Fig. 5(a)), corroborating the occurrence of a phase transition between orthorhombic and tetragonal structures[4,14] during this specific voltage window. These *operando* XRD results provide direct evidence of the reversible structural changes in YTOS, demonstrating its ability to sustain stable Li^+ intercalation without significant structural collapse or degradation.

Fig. 7 presents *operando* Ti K-edge X-ray absorption fine structure (XAFS) spectra of YTOS recorded during the 1st cycle [top] and the 500th cycle [bottom], alongside Y K-edge spectra. These measurements provide insights into the evolution of the electronic structure and local coordination environment of Ti and Y during electrochemical cycling. During the initial charge–discharge cycle, the Ti K-edge spectra exhibit a reversible energy shift correlated with changes in the oxidation state of Ti. At 0.1 V *vs.* Li/Li^+, the absorption edge shifts toward lower energy, indicative of the presence of Ti^{3+}, while at 3.0 V *vs.* Li/Li^+, the edge shifts toward higher energy, corresponding to Ti^{4+}. This reversible energy modulation confirms a Ti^{3+}/Ti^{4+} redox process, which governs the lithiation and delithiation of YTOS, in line with prior observations for Ti-based anode materials such as anatase TiO_2,[23,24] bronze TiO_2,[25,26] $Li_4Ti_5O_{12}$,[27–29] $TiNb_2O_7$,[30] and $Li_2ZnTi_3O_8$.[31] Among those Ti-based anode materials, YTOS exhibits a low reaction potential range (0.1–1.5 V *vs.* Li/Li^+), owing to the low Ti d-band due to the mixed anion (O^{2-}/S^{2-}) environment.[4,11] Additionally, the pre-edge region at approximately 4968 eV, associated with the 1s → 3d transition,[32,33] exhibits a diminished intensity. This reduction in pre-edge features suggests changes in the local coordination environment, specifically alterations in the symmetry surrounding Ti within the TiO_5S octahedral framework (see Fig. 7 inset). The observed recovery of electronic symmetry is consistent with the *operando* XRD results shown in Fig. 6, which indicate that during electrochemical cycling, the vertical TiO_5S octahedron undergoes contraction along the *c*-axis due to Ti–S bonding. This contraction effectively enhances the

crystallographic isotropy of the structure, further reinforcing the stability of the material. Importantly, the Ti K-edge spectra for the 500th cycle reveal a similar reversible energy shift, confirming the sustained redox reversibility of Ti^{3+}/Ti^{4+} even after extensive cycling. This finding highlights the structural integrity and electrochemical resilience of YTOS, as further corroborated by long-term cycling performance data presented in Fig. 4 [Right]. The minimal degradation in redox activity over 500 cycles indicates that the electronic and structural reversibility of Ti remains well-preserved (Fig. S5). In contrast to the pronounced spectral shifts observed at the Ti K-edge, the Y K-edge measured at 0.1 V (red; reduced state) and 3.0 V (blue; oxidized state) are essentially superimposable across the edge jump region (17 000–17 050 eV), demonstrating that the Y oxidation state remains unchanged over the entire operating potential window. The lack of significant changes at the Y K-edge further reinforces the notion that the Y sites primarily function as structural stabilizers rather than active redox centers. The obtained *operando* XRD supports the idea, revealing a reversible shift of the (004) reflection (see Fig. 6), consistent with *c*-axis contraction/expansion during (de)lithiation. The overall volume change is small (<5%),[14] indicating that the Y_2S_2 rock-salt layers accommodate interlayer shear and strain, thereby maintaining structural integrity during cycling. Furthermore, first-principle simulation reports on YTOS show that the valence-band maximum is dominated by S 3p states, the conduction-band minimum (CBM) is Ti 3d dominated, and Y 5d states lie several eV above the CBM (~4 eV).[2,34] This confirms that Y makes negligible contributions near the Fermi level, reinforcing its role as a redox-inert framework stabilizing the Ti-centered redox. These *operando* XAFS results, together with complementary XRD analysis, provide strong evidence that YTOS maintains its redox reversibility and structural stability even after prolonged cycling. For comparison, other layered oxysulfides, such as the $Sr_2MnO_2Cu_{4-\delta}S_3$ family,[35,36] store Li through conversion–alloying reactions involving Cu extrusion/reinsertion. These processes entail large structural reorganization, significant hysteresis, and greater volume change. In contrast, YTOS undergoes Ti-centered intercalation supported by the Y-based scaffold, explaining its minimal lattice hysteresis and superior cycling durability.

Long-term stability for YTOS||AC full cells

To evaluate the practical applicability of YTOS as a negative electrode in hybrid supercapacitors, full-cell performance tests were conducted using a YTOS||AC configuration. Fig. 8 presents the electrochemical performance of the full cell, including long-term cycling stability, polarization behavior, and voltage profiles at varying current densities. The full cell maintains excellent capacity retention even after prolonged cycling under high-rate charge–discharge conditions. The applied current density was 10C/10C, ensuring that the system was tested under demanding operating conditions. Despite the high charge–discharge rates, the full cell exhibited minimal capacity fading over 10 000 cycles, highlighting structural stability and

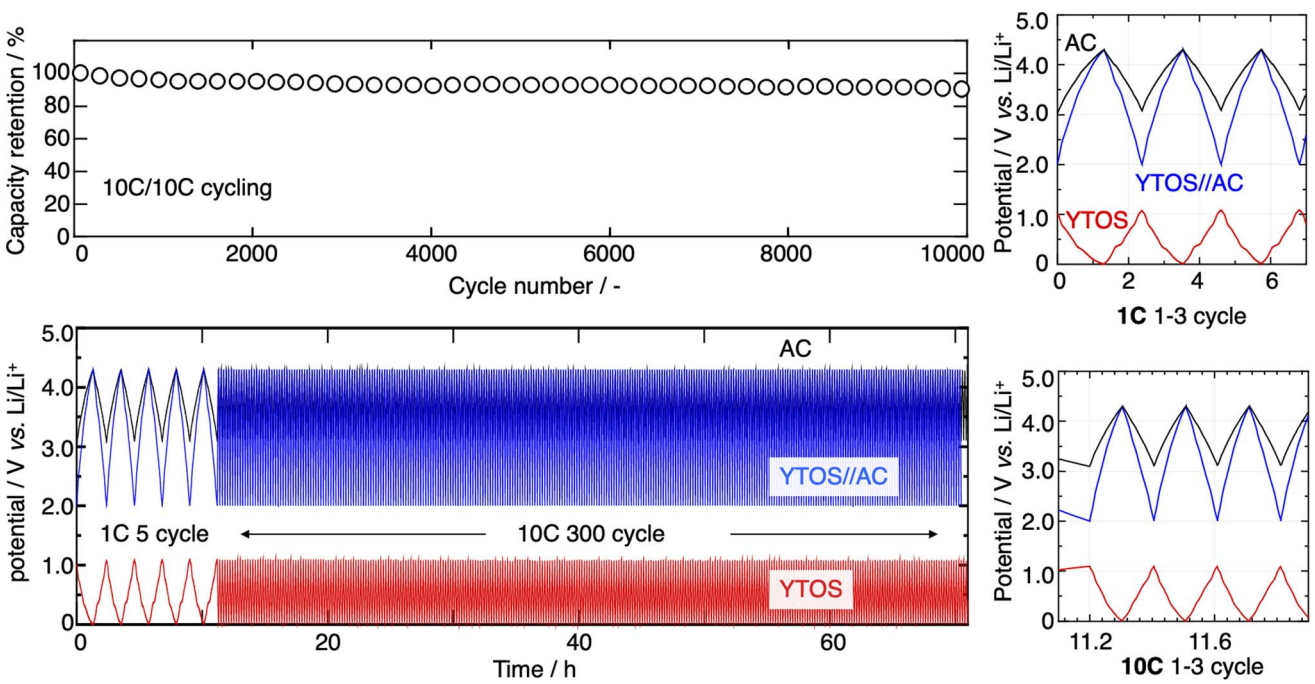

Fig. 8 Excellent stability of YTOS||AC full cell performance using 1 M$LiBF_4$/EC + DMC (50 : 50 in vol%). [Top left] Capacity retention plots of YTOS||AC full cell over 10 000 cycles. Applied current density was fixed at 10C/10C. [Bottom left] Monitored polarization curves of YTOS negative and AC positive electrodes using Li reference electrode, along with voltage curves of YTOS||AC full cell, at the current density 1C/1C and 10C/10C. [Right] Enlarged polarization curves at 1C/1C [Top] and 10C/10C [Bottom]. In both cases, the typical characteristics of YTOS polarization curves, featuring a gentle slope with multiple stepped plateaus, were observed. No significant difference in overpotential was noted by increasing current density (10C), confirming stable operation as a YTOS||AC hybrid capacitor.

electrochemical reversibility of YTOS. Polarization curves were recorded separately for the YTOS negative electrode and the AC positive electrode *versus* a Li metal reference electrode (Fig. 8 [Bottom left]). The polarization behavior was monitored at two different current densities: 1C/1C and 10C/10C. The voltage profiles of the YTOS||AC full cell are displayed alongside, enabling a direct comparison of the electrode performance. The recorded polarization curves provide valuable information about the charge transfer resistance, reaction kinetics, and overall energy efficiency of the system.

A more detailed analysis of the polarization behavior is also shown in Fig. 8 [Right], where enlarged polarization curves at 1C/1C [top] and 10C/10C [bottom] are presented. A key observation from these plots is the characteristic polarization behavior of YTOS, which exhibits a gentle slope with multiple stepped plateaus. These features suggest a complex but highly stable Li^+ insertion/extraction mechanism, possibly involving multiple lithiation sites or phase transitions within the YTOS structure. Importantly, despite the increase in current density from 1C to 10C, the overpotential of the YTOS electrode does not exhibit significant changes. This indicates that the charge transport and reaction kinetics remain efficient even at high charge–discharge rates, reinforcing the idea that YTOS possesses outstanding rate capability. The ability to maintain low polarization at higher current densities is crucial for practical applications, as it ensures that the electrode can deliver high power without significant energy losses. Such excellent cyclability is comparable to other representative state-of-the-art hybrid supercapacitors as summarized in Table S2. For Ti-based anodes, benchmark data include TiO_2(B)||AC[39] and $Li_4Ti_5O_{12}$||AC,[40] which are renowned for high rate capability and excellent cyclability but are typically constrained by modest specific energy owing to high working potentials and limited capacity. Li_3VO_4||AC[41] offers higher capacity and thus higher specific energy, yet often suffers from inferior long-term stability linked to structural degradation. More recently, disordered-rock-salt (DRX) – $Li_3V_2O_5$ (ref. 42) has been explored to alleviate these trade-offs, although pronounced voltage hysteresis and synthetic complexity persist. Against these benchmarks, the YTOS||AC cell demonstrates a unique balance of high energy density, minimal voltage hysteresis, and excellent capacity retention over extended cycling, underscoring the distinct advantage conferred by the Y-stabilized Ti-centered intercalation mechanism.

Conclusions

This work demonstrates the viability of $Y_2Ti_2O_5S_2$ (YTOS) as a high-performance anode material for hybrid supercapacitors. The layered RP framework of YTOS, composed of alternating $[TiO_5S]$ perovskite-like slabs and $[Y_2S_2]^{2+}$ rock-salt layers, affords high electronic conductivity and rapid Li^+ diffusion through its anisotropic architecture. Electrochemical testing revealed that bulk YTOS electrodes—enhanced by the incorporation of 1 wt% SWCNTs—exhibited a high specific capacity of 121 mA h g^{-1} (95% of the theoretical value), exceptional rate capability up to 230C, and 95% capacity retention after 1000 cycles.

Operando XRD and Ti K-edge XAFS analyses confirmed a fully reversible orthorhombic–tetragonal phase transition and robust Ti^{3+}/Ti^{4+} redox reversibility over 500 cycles, while Y K-edge spectra remained unchanged, validating the structural stability provided by the Y sublattice. Kinetic analysis using GITT and cavity microelectrode voltammetry revealed fast Li^+ transport with diffusion coefficients ranging from 10^{-9} to 10^{-11} cm^2 s^{-1}, and a surface-to-diffusion transition boundary above 0.25 $V^{1/2}$ $s^{-1/2}$—surpassing conventional Ti-based anode materials.

Furthermore, YTOS||AC full cells maintained stable cycling over 10 000 cycles at 10C with minimal polarization, confirming the composite's applicability in high-power configurations. These findings underscore the structural resilience, kinetic favorability, and dual ionic–electronic conductivity of YTOS, offering a compelling platform for durable, fast-charging energy storage applications. Future optimization of electrode formulation and electrolyte compatibility may further enhance its potential.

Author contributions

Etsuro Iwama: conceptualization, data curation, investigation, supervision, validation, writing – original draft, writing – review & editing. Shintaro Aoyagi: conceptualization, data curation, investigation, methodology. Tatsuro Aoyama: investigation, methodology. Ami Kudo: investigation, methodology. Keita Okazaki: investigation, methodology. Daichi Akiyama: investigation, methodology. Keisuke Matsumura: conceptualization, data curation, investigation, writing – original draft, writing – review & editing. Naohisa Okita: data curation, supervision, writing – review & editing. Kazuaki Kisu: conceptualization, investigation, methodology, supervision. Wako Naoi: investigation, visualization, writing – original draft. Patrick Rozier: data curation, validation, writing – review & editing. Patrice Simon: data curation, validation, writing – review & editing. Katsuhiko Naoi: conceptualization, funding acquisition, project administration, supervision, writing – review & editing.

Conflicts of interest

The authors declare that they have no known competing financial interests or personal relationships that could have appeared to influence the work reported in this paper.

Data availability

Any additional information can be obtained from the corresponding authors upon request.

The data that support the findings of the present study are available in this article and its supplementary information (SI). Supplementary information: a conceptual illustration of YTOS (Fig. S1); a TGA curve (Fig. S2); STEM images with overlaid elemental maps (Fig. S3); XPS spectra (Fig. S4); charge–discharge curves of YTOS without SWCNTs (Fig. S5); *ex situ* XRD patterns and Ti K-edge spectra of YTOS after 500 cycles (Fig. S6); voltage-relaxation traces during GITT (Fig. S7); dQ/dV plots (Fig.

S8); a literature survey of electrochemical performance of YTOS for Li-ion storage (Table S1); and representative performance metrics for hybrid supercapacitors (Table S2). See DOI: https://doi.org/10.1039/d5ta05379j.

Acknowledgements

This study was supported by the Global Innovation Research Organization in TUAT, JSPS Grant-in-Aid for Scientific Research (KAKENHI) A under Grant No. JP25H00858, and Grant-in-Aid for Early-Career Scientists under Grant No. JP25K17826.

References

1 S. G. Denis and S. J. Clarke, *Chem. Commun.*, 2001, 2356–2357.
2 K. McColl and F. Corà, *J. Mater. Chem. A*, 2021, **9**, 7068–7084.
3 V. Nandal, R. Shoji, H. Matsuzaki, A. Furube, L. Lin, T. Hisatomi, M. Kaneko, K. Yamashita, K. Domen and K. Seki, *Nat. Commun.*, 2021, **12**, 7055.
4 G. Hyett, O. J. Rutt, Z. A. Gál, S. G. Denis, M. A. Hayward and S. J. Clarke, *J. Am. Chem. Soc.*, 2004, **126**, 1980–1991.
5 Y. Yao, Q. Li, W. Chu, Y.-m. Ding, L. Yan, Y. Gao, A. Neogi, A. Govorov, L. Zhou and Z. Wang, *Phys. Chem. Chem. Phys.*, 2023, **25**, 32875–32882.
6 Q. Wang, M. Nakabayashi, T. Hisatomi, S. Sun, S. Akiyama, Z. Wang, Z. Pan, X. Xiao, T. Watanabe, T. Yamada, N. Shibata, T. Takata and K. Domen, *Nat. Mater.*, 2019, **18**, 827–832.
7 K. Brlec, K. B. Spooner, J. M. Skelton and D. O. Scanlon, *J. Mater. Chem. A*, 2022, **10**, 16813–16824.
8 Y. Yao, Q. Li, Y.-m. Ding, L. Yan, W. Chen, A. Govorov, Z. Wang and L. Zhou, *J. Phys. Chem. Lett.*, 2023, **14**, 9075–9081.
9 S. J. Clarke, S. G. Denis, O. J. Rutt, T. L. Hill, M. A. Hayward, G. Hyett and Z. A. Gál, *Chem. Mater.*, 2003, **15**, 5065–5072.
10 O. J. Rutt, T. L. Hill, Z. A. Gál, M. A. Hayward and S. J. Clarke, *Inorg. Chem.*, 2003, **42**, 7906–7911.
11 H. Oki and H. Takagi, *Solid State Ionics*, 2015, **276**, 80–83.
12 W. Schmidt, P. Bottke, M. Sternad, P. Gollob, V. Hennige and M. Wilkening, *Chem. Mater.*, 2015, **27**, 1740–1750.
13 W. Zhang, D.-H. Seo, T. Chen, L. Wu, M. Topsakal, Y. Zhu, D. Lu, G. Ceder and F. Wang, *Science*, 2020, **367**, 1030–1034.
14 N. Takada, A. Nasu, H. Kobayashi and M. Matsui, *Electrochemistry*, 2025, **93**, 063018.
15 S. Ishimoto, Y. Asakawa, M. Shinya and K. Naoi, *J. Electrochem. Soc.*, 2009, **156**, A563–A571.
16 L. Lin, M. Nakabayashi, D. Lu, T. Hisatomi, T. Takata and K. Domen, *Chem. Mater.*, 2024, **36**, 1612–1620.
17 K. Brlec, C. N. Savory and D. O. Scanlon, *J. Mater. Chem. A*, 2023, **11**, 16776–16787.
18 W. Weppner and R. A. Huggins, *J. Electrochem. Soc.*, 1977, **124**, 1569.
19 W. Weppner and R. A. Huggins, *J. Solid State Chem.*, 1977, **22**, 297–308.
20 J. Come, P. L. Taberna, S. Hamelet, C. Masquelier and P. Simon, *J. Electrochem. Soc.*, 2011, **158**, A1090–A1093.
21 K. Naoi, T. Kurita, M. Abe, T. Furuhashi, Y. Abe, K. Okazaki, J. Miyamoto, E. Iwama, S. Aoyagi, W. Naoi and P. Simon, *Adv. Mater.*, 2016, **28**, 6751–6757.
22 K. Kisu, E. Iwama, W. Naoi, P. Simon and K. Naoi, *Electrochem. Commun.*, 2016, **72**, 10–14.
23 D.-H. Lee, B.-H. Lee, A. K. Sinha, J.-H. Park, M.-S. Kim, J. Park, H. Shin, K.-S. Lee, Y.-E. Sung and T. Hyeon, *J. Am. Chem. Soc.*, 2018, **140**, 16676–16684.
24 M. García-Tecedor, G. Gorni, F. Oropeza, L. Gómez, M. Liras, V. A. de la Peña O'Shea and M. Barawi, *J. Mater. Chem. A*, 2022, **10**, 19994–20004.
25 M. Fehse, M. Ben Yahia, L. Monconduit, F. Lemoigno, M.-L. Doublet, F. Fischer, C. Tessier and L. Stievano, *J. Phys. Chem. C*, 2014, **118**, 27210–27218.
26 Y. Tang, Y. Zhang, O. I. Malyi, N. Bucher, H. Xia, S. Xi, Z. Zhu, Z. Lv, W. Li, J. Wei, M. Srinivasan, A. Borgna, M. Antonietti, Y. Du and X. Chen, *Adv. Mater.*, 2018, **30**, 1802200.
27 M. Venkateswarlu, C. H. Chen, J. S. Do, C. W. Lin, T. C. Chou and B. J. Hwang, *J. Power Sources*, 2005, **146**, 204–208.
28 K. Mukai, T. Nonaka and T. Uyama, *Energy Storage Mater.*, 2022, **44**, 547–556.
29 S. Kim, S. Fang, Z. Zhang, J. Chen, L. Yang, J. E. Penner-Hahn and A. Deb, *J. Power Sources*, 2014, **268**, 294–300.
30 Y. Son, H. Jang, B. Wen, C. Jo, A. S. Groombridge, A. Boies, M. G. Kim and M. De Volder, *J. Mater. Chem. A*, 2025, **13**, 9878–9885.
31 K. Mukai, T. Uyama and T. Nonaka, *Inorg. Chem.*, 2023, **62**, 5602–5613.
32 T. Yamamoto, *X-Ray Spectrom.*, 2008, **37**, 572–584.
33 T. E. Westre, P. Kennepohl, J. G. DeWitt, B. Hedman, K. O. Hodgson and E. I. Solomon, *J. Am. Chem. Soc.*, 1997, **119**, 6297–6314.
34 J. Zhang, K. Liu, B. Zhang, J. Zhang, M. Liu, Y. Xu, K. Shi, H. Wang, Z. Zhang, P. Zhou and G. Ma, *J. Am. Chem. Soc.*, 2024, **146**, 4068–4077.
35 S. Indris, J. Cabana, O. J. Rutt, S. J. Clarke and C. P. Grey, *J. Am. Chem. Soc.*, 2006, **128**, 13354–13355.
36 S. Dey, D. Zeng, P. Adamson, J. Cabana, S. Indris, J. Lu, S. J. Clarke and C. P. Grey, *Chem. Mater.*, 2021, **33**, 3989–4005.
37 S. Liu, G. R. Odette and C. U. Segre, *J. Nucl. Mater.*, 2014, **445**, 50–56.
38 P. He, T. Liu, A. Möslang, R. Lindau, R. Ziegler, J. Hoffmann, P. Kurinskiy, L. Commin, P. Vladimirov, S. Nikitenko and M. Silveir, *Mater. Chem. Phys.*, 2012, **136**, 990–998.
39 T. Brousse, R. Marchand, P.-L. Taberna and P. Simon, *J. Power Sources*, 2006, **158**, 571–577.
40 G. G. Amatucci, F. Badway, A. Du Pasquier and T. Zheng, *J. Electrochem. Soc.*, 2001, **148**, A930.
41 S.-C. Hsu, K.-S. Wang, Y.-T. Lin, J.-H. Huang, N.-J. Wu, J.-L. Kang, H.-C. Weng and T.-Y. Liu, *Polymers*, 2023, **15**, 2502.
42 Y. Qin, H. Zhao, M. Hua, J. Gao, J. Lu, S. Zhang, X. Lin, J. Sun, L. Yin and R. Wang, *J. Power Sources*, 2023, **588**, 233722.

